Last Glacial Maximum temperature in the Alps quantified using luminescence paleothermometry

Rabiul Biswas, Vjeran Višnjević, Florence Magnin, Benjamin Lehmann, Georgina King, Frédéric Herman

To cite this version:

Rabiul Biswas, Vjeran Višnjević, Florence Magnin, Benjamin Lehmann, Georgina King, et al.. Last Glacial Maximum temperature in the Alps quantified using luminescence paleothermometry. 2020. ⟨hal-03024184⟩

HAL Id: hal-03024184
https://hal.science/hal-03024184v1

Preprint submitted on 25 Nov 2020

Last Glacial Maximum temperature in the Alps quantified using luminescence paleothermometry

Rabiul Biswas[1], Vjeran Višnjević[1], Florence Magnin[2], Benjamin Lehmann[1], Georgina King[1], Frédéric Herman[1]

Corresponding author: frederic.herman@unil.ch

[1]: Institute of Earth Surface dynamics, University of Lausanne, Switzerland

[2]: Laboratoire EDYTEM, Université Savoie Mont-Blanc, France

The Last Glacial Maximum (LGM) corresponds to the most recent time when ice-sheets and ice-caps globally reached their maximum integrated volume. Quantifying how cold it was remains challenging, especially in regions that were entirely covered by ice. Climate records are often not well preserved, thereby restricting the use of existing climate proxies. Here we demonstrate that the mean annual temperature in the western Alps was 8.8 ± 2.1 °C cooler at the end of the LGM than present by measuring the temperature history recorded in rocks using thermoluminescence of feldspar. These results are consistent with climatic reconstructions inferred from the detailed geomorphic mapping of the ice-cap that covered the Alps. Our results imply that climate was considerably colder than the global average and substantially drier in central western Europe compared to present.

The Last Glacial Maximum (LGM) lasted from about 33 kyr to about 17 kyr ago and corresponds to the largest and probably best-documented climate change in recent Earth history (*1*). Climate was generally drier and temperatures were globally lower. Cooling led to the expansion of polar ice-sheets and icecaps at high latitudes and on sufficiently high mountain ranges, but what the actual temperature was during the LGM remains uncertain. Despite a long history of research (*2*), estimates of mean global temperature vary widely from 1.7 to 8 °C lower than present (*3-9*). In addition, such global temperatures mask even larger regional temperature fluctuations. Quantifying regional variations is particularly important to understand climate dynamics as regional temperature differences cause pressure gradients that govern the distribution of heat and moisture on Earth.

In that context, the LGM European continental climate is particularly elusive. Temperature and precipitation in western Europe are primarily controlled by the position and intensity of the jet stream and storm track. The decrease of greenhouse gas concentrations in the atmosphere and the presence of large ice sheets during the LGM caused a decrease in temperature that increases with increasing latitude. Such a strengthening of the equator to pole temperature gradient likely affected the position and intensity of the jet stream and storm track, and thus European climate. This problem has been the focus of numerous modeling studies (*10-14*), which often argue for a more zonally oriented atmospheric jet stream during the LGM compared to present (*12,15*) but predict surprisingly different temperature and precipitation patterns over western Europe (*11,13,14*). These differences are even further exacerbated by their longstanding disagreement (*10,14*) with climate reconstructions based on pollen (*16-18*) or stable isotope in groundwater (*19*) and speleothems (*20*).

The western Alps host the highest topography in central western Europe and form an important physical boundary that strongly influences the climate of surrounding regions. During the LGM, the Alps were entirely covered by a large ice-cap that reflected climatic conditions in Europe at that time (*21-23*). The ice extent reflects temperature, precipitation and insolation, but the ensemble of temperature and precipitation combinations that can explain the observed ice extent is non-unique and varies spatially (*22*). Furthermore, there still exist large uncertainties concerning the ice thickness (*23*) although the ice extent is well documented (*24*). As a result, it is not possible to discriminate precipitation and temperature changes using the ice extent alone. One must acquire independent estimates of temperature or precipitation to constrain the climatic conditions that prevailed in central Europe during the LGM.

To independently constrain how temperature changed between the LGM and the present, we collected samples along a 500 m vertical profile on the valley flanks of the Mer de Glace, one of the largest glaciers in the Alps which retreated since about 19-17 kyr ago (*25-26*). We collected samples on steep slopes, which only accumulate limited amounts of snow in winter (Fig. 1). The rocks have been exposed to atmospheric conditions since the end of LGM and thus provide a record of atmospheric temperature since that time. We reconstructed the temperature history of each rock using a new method based on thermoluminescence of feldspar (*27*). The principle of the approach consists of translating the abundance of trapped electrons in the crystalline lattice into corresponding time-temperature histories (*27*; Supplementary Materials). Using a well-calibrated physical model combined with a Bayesian approach, we reconstruct the mean annual temperature since the end of the LGM. In comparison to other existing proxies, our method does not rely on numerous climatic assumptions such as seasonality, precipitation, plant-available moisture, the length of the growing season (*16-18*) or the preservation of organic compounds (*28*).

Our results show that the temperature difference between the LGM and the present is about 9 °C for all samples (Fig. 2). The thermoluminescence method yields rock temperatures that are higher than atmospheric mean annual temperatures. However, it is expected that the temperature in rocks exhibit an offset with atmospheric temperature depending on their exposure to solar radiation, their color and the amount of snow cover (*29*). We compare our results to temperatures estimated from a statistical relationship between air temperature and measured rock temperature used to characterize rock permafrost (*29*). The results show a good match between the two approaches (Fig. 2). Combining all the luminescence measurements, we find a temperature difference between the LGM and the present of 8.8 ± 2.1 °C. The constant temperature difference with altitude also indicates that the lapse rate did not change between the LGM and today, and remained about 0.55 ˚C per 100 m.

Višnjević et al. (*22*) recently inverted the ice extent for the entire Alps into spatially variable equilibrium line altitudes (ELAs) (Supplementary Materials). The ELA is the most useful parameter to quantify the effect of climate on glaciers and icecaps. It defines the altitude where the annual accumulation of snow is equal to the ablation, and it primarily depends on winter precipitation and mean annual temperature. They ran 25 inversions (*22*) that we complement with 12 additional inversions to find the ELA maps (Fig. 3) that best explain the observed ice extent. Then we translate the LGM ELA maps into mean annual temperatures and winter accumulation rates at the Mer de Glace, using the prescribed accumulation rate and our observation that the altitudinal temperature lapse rate did not change between the end of the LGM and the present (Supplementary Materials). The temperature histories inferred from thermoluminescence are local but the inversion of the ice extent enables us to integrate information at the scale of the Alps. Furthermore, our calculations illustrate the tradeoff that exists between temperature and precipitation when using the past ice extent as sole information (*22-23*).

The combination of our results imply that climate in the Alps was colder at the end of the LGM by about 9°C and more likely between 50 and 85% drier than it currently is (Fig. 4). The estimated temperature difference also matches the results from an independent ice-extent reconstruction that assumes that precipitation patterns at the LGM were identical to present but that climate was about 50% drier (*23*). More importantly, temperatures in the Alps at the end of the LGM were cooler than the recently estimated -6.1 °C global cooling (*9*). Estimates of global averages are overwhelmingly based on marine sea surface temperature records and models. Our results imply that temperature differences between the end of the LGM and the present can be larger in regions that were entirely covered by ice. If these locations were included, estimated global average temperature would be lower.

Inferences of past climate in the Alps have so far relied on the analysis of fossil assemblages of biota and pollen preserved in lake sediments and peat (*30*), the analysis of oxygen isotopes in speleothems (e.g., *20*), lake sediments (e.g., *31*) and groundwater (*19*), or the analysis of past soil formation processes (*30*). Although the existing records show that climate in the Alps likely followed the Greenland oxygen isotope record (*30*), there is currently no climate record that span the last 20 kyr continuously. The ice-cap that covered the Alps prevented vegetation to grow and thereby produce the necessary climate archive. Additionally, uncertainties on the atmospheric conditions during the LGM have made the conversion of most climate proxies into LGM temperature and precipitation particularly challenging (*30*). The fossil pollen records suggest that the mean annual temperature difference between the LGM and today is somewhere between 10 and 15 °C (*16,18*). Our results provide us with slightly lower temperature estimates. Interestingly, lower temperature differences are in better agreement with existing climate simulations (*10,14*).

Our findings that temperatures at the end of the LGM were 8.8 ± 2.1 °C lower than present and possibly up to 85% drier suggest that an increase of moisture related to a large southward shift of the storm track trajectories that would lead to an increase of atmospheric moisture in the Alps is rather unlikely (*20,21*). Instead, our results are more consistent with a range of atmospheric models (*14*) and in particular those suggesting a more zonally oriented atmospheric jet stream and storm track during the LGM (*12,15*). These models predict a southward shift of the jet stream that only extended south of the Scandinavian ice cap (*12*) and primarily happened in summer (*11*) during the LGM.

References

1. Clark, P.U., Dyke, A.S., Shakun, J.D., Carlson, A.E., Clark, J., Wohlfarth, B., Mitrovica, J.X., Hostetler, S.W., McCabe, A.M. The last glacial maximum. *Science*, ***325*****(5941),** 710-714 (2009).
2. CLIMAP Project Members. The surface of the ice-age earth. *Science*, **191(4232)**, 1131-1137 (1976).
3. Schneider von Deimling, T., Ganopolski, A., Held, H. & Rahmstorf, S. How cold was the last glacial maximum? *Geophysical Research Letters*, ***33*****(14)** (2006).
4. Holden, P.B., Edwards, N.R., Oliver, K.I.C., Lenton, T.M., Wilkinson, R.D.. A probabilistic calibration of climate sensitivity and terrestrial carbon change in GENIE-1. *Climate Dynamics*, *35*(5), 785-806 (2010).
5. Schmittner, A., Urban, N.M., Shakun, J.D., Mahowald, N.M., Clark, P.U., Bartlein, P.J., Mix, A.C., Rosell-Melé, A.. Climate sensitivity estimated from temperature reconstructions of the Last Glacial Maximum. *Science*, ***334*****(6061)**, 1385-1388 (2011).
6. Shakun, J.D., Clark, P.U., He, F., Marcott, S.A., Mix, A.C., Liu, Z., Otto-Bliesner, B., Schmittner, A., Bard, E.. Global warming preceded by increasing carbon dioxide concentrations during the last deglaciation. *Nature*, ***484*****(7392)**, 49-54 (2012).
7. Annan, J.D. and Hargreaves, J.C.. A new global reconstruction of temperature changes at the Last Glacial Maximum. *Climate of the Past*, ***9*****(1)**, 367-376 (2013).
8. Bereiter, B., Shackleton, S., Baggenstos, D., Kawamura, K., Severinghaus, J. Mean global ocean temperatures during the last glacial transition. *Nature*, ***553*****(7686)**, 39-44 (2018).
9. Tierney, J. E., Zhu, J., King, J., Malevich, S. B., Hakim, G., & Poulsen, C. Glacial cooling and climate sensitivity revisited. *Nature*, (in press)
10. Kageyama, M., Laîné, A., Abe-Ouchi, A., Braconnot, P., Cortijo, E., Crucifix, M., De Vernal, A., Guiot, J., Hewitt, C.D., Kitoh, A., Kucera, M. Last Glacial Maximum temperatures over the North Atlantic, Europe and western Siberia: a comparison between PMIP models, MARGO sea–surface temperatures and pollen-based reconstructions. *Quaternary Science Reviews*, ***25*****(17-18)**, 2082-2102 (2006).
11. Beghin, P., Charbit, S., Kageyama, M., Combourieu-Nebout, N., Hatté, C., Dumas, C., Peterschmitt, J.Y. What drives LGM precipitation over the western Mediterranean? A study focused on the Iberian Peninsula and northern Morocco. *Climate Dynamics*, ***46*****(7-8)**, 2611-2631 (2016).
12. Löfverström, M., Caballero, R., Nilsson, J., Messori, G. Stationary wave reflection as a mechanism for zonalizing the Atlantic winter jet at the LGM. *Journal of the Atmospheric Sciences*, ***73*****(8)**, 3329-3342 (2016).
13. Ludwig, P., Schaffernicht, E.J., Shao, Y., Pinto, J.G. Regional atmospheric circulation over Europe during the Last Glacial Maximum and its links to precipitation. *Journal of Geophysical Research: Atmospheres*, ***121*****(5)**, 2130-2145 (2016).
14. Kageyama, M., Harrison, S.P., Kapsch, M.L., Löfverström, M., Lora, J.M., Mikolajewicz, U., Sherriff-Tadano, S., Vadsaria, T., Abe-Ouchi, A., Bouttes, N., Chandan, D. The PMIP4-CMIP6 Last Glacial Maximum experiments: preliminary results and comparison with the PMIP3-CMIP5 simulations. *Climate of the Past Discussions* (2020)

15. Li, C., Battisti, D.S.. Reduced Atlantic storminess during Last Glacial Maximum: Evidence from a coupled climate model. *Journal of Climate*, *21*(14), 3561-3579 (2008).
16. Peyron, O., Guiot, J., Cheddadi, R., Tarasov, P., Reille, M., de Beaulieu, J.L., Bottema, S., Andrieu, V., 1998. Climatic reconstruction in Europe for 18,000 yr BP from pollen data. *Quaternary research*, ***49*****(2)**, 183-196 (1998).
17. Bartlein, P.J., Harrison, S.P., Brewer, S., Connor, S., Davis, B.A.S., Gajewski, K., Guiot, J., Harrison-Prentice, T.I., Henderson, A., Peyron, O., Prentice, I.C. Pollen-based continental climate reconstructions at 6 and 21 ka: a global synthesis. *Climate Dynamics*, ***37*****(3)**, 775-802 (2011).
18. Wu, H., Guiot, J., Brewer, S., Guo, Z. Climatic changes in Eurasia and Africa at the last glacial maximum and mid-Holocene: reconstruction from pollen data using inverse vegetation modelling. *Climate Dynamics*, ***29*****(2-3)**, 211-229 (2007).
19. Beyerle, U., Purtschert, R., Aeschbach-Hertig, W., Imboden, D.M., Loosli, H.H., Wieler, R., Kipfer, R. Climate and groundwater recharge during the last glaciation in an ice-covered region. *Science*, ***282*****(5389)**, 731-734 (1998).
20. Luetscher, M., Boch, R., Sodemann, H., Spötl, C., Cheng, H., Edwards, R.L., Frisia, S., Hof, F., Müller, W. North Atlantic storm track changes during the Last Glacial Maximum recorded by Alpine speleothems. *Nature Communications*, ***6*****(1)**, 1-6 (2015).
21. Florineth, D., Schlüchter, C. Reconstructing the Last Glacial Maximum (LGM) ice surface geometry and flowlines in the Central Swiss Alps. *Eclogae Geologicae Helvetiae*, ***91***, 91-407 (1998).
22. Višnjević, V., Herman, F., Prasicek, G. Climatic patterns over the European Alps during the LGM derived from inversion of the paleo-ice extent. *Earth and Planetary Science Letters*, ***538***, 116-185 (2020).
23. Seguinot, J., Ivy-Ochs, S., Jouvet, G., Huss, M., Funk, M., Preusser, F. Modelling last glacial cycle ice dynamics in the Alps. *The Cryosphere*, ***12*****(10)**, 3265-3285 (2018).
24. Ehlers, J., Gibbard, P.L., Hughes, P.D. *Quaternary glaciations-extent and chronology: a closer look* (Vol. 15). Elsevier. (2011)
25. Wirsig, C., Zasadni, J., Christl, M., Akçar, N., Ivy-Ochs, S. Dating the onset of LGM ice surface lowering in the High Alps. *Quaternary Science Reviews*, ***143***, 37-50 (2016).
26. Lehmann, B., Herman, F., Valla, P.G., King, G.E., Biswas, R.H., Ivy-Ochs, S., Steinemann, O., Christl, M.. Postglacial erosion of bedrock surfaces and deglaciation timing: New insights from the Mont Blanc massif (western Alps). *Geology*, ***48*****(2)**, 139-144 (2020).
27. Biswas, R.H., Herman, F., King, G.E., Lehmann, B., Singhvi, A.K. Surface paleothermometry using low temperature thermoluminescence of feldspar. *Climate of the Past Discussions*, 1-26 (2020).
28. Schouten, S., Hopmans, E.C., Damsté, J.S.S.. The organic geochemistry of glycerol dialkyl glycerol tetraether lipids: a review. *Organic geochemistry*, ***54***, 19-61 (2013).
29. Magnin, F., Deline, P., Ravanel, L., Noetzli, J., Pogliotti, P. Thermal characteristics of permafrost in the steep alpine rock walls of the Aiguille du Midi (Mont Blanc Massif, 3842 m asl). *The Cryosphere*, ***9*****(1)**, 109-121 (2015).
30. Heiri, O., Koinig, K.A., Spötl, C., Barrett, S., Brauer, A., Drescher-Schneider, R., Gaar, D., Ivy-Ochs, S., Kerschner, H., Luetscher, M., Moran, A. Palaeoclimate

records 60–8 ka in the Austrian and Swiss Alps and their forelands. *Quaternary Science Reviews*, ***106***, 186-205 (2014).

31. Lauterbach, S., Brauer, A., Andersen, N., Danielopol, D.L., Dulski, P., Hüls, M., Milecka, K., Namiotko, T., Obremska, M., Von Grafenstein, U., Declakes Participants. Environmental responses to Lateglacial climatic fluctuations recorded in the sediments of pre-Alpine Lake Mondsee (northeastern Alps). *Journal of Quaternary Science*, ***26*****(3)**, 253-267 (2011).

Acknowledgements

The authors Basil Davis for discussions and feedback on the manuscript. The luminescence data and codes are available on https://github.com/cirederf13/TL_paleothermometry. The data and code for the inversion of past ice extents into ELA are available on XXX. Temperature data used to estimate rock temperature are available on XXX.

Figures

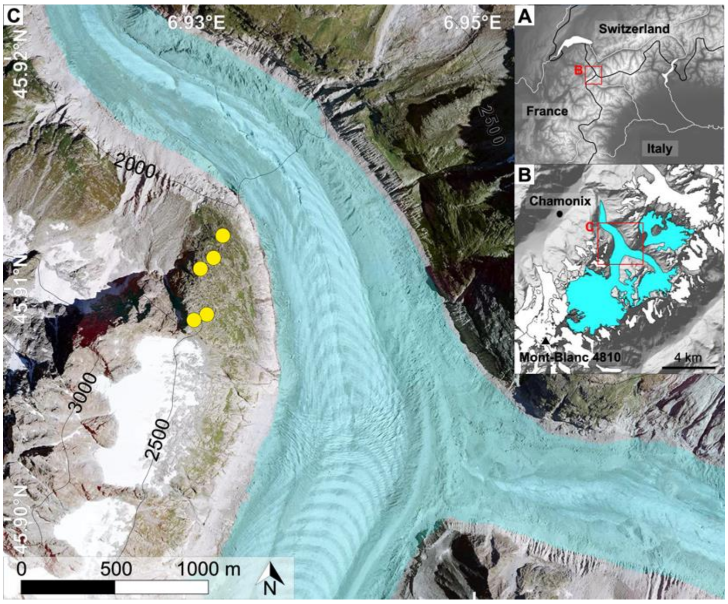

Figure 1: Samples location. (A) Digital elevation model of the Alps. (B) Mont Blanc Massif. (C) Mer de Glace. The yellow dots show the location of the analyzed samples. The red boxes in (A) and (B) show the location of (B) and (C).

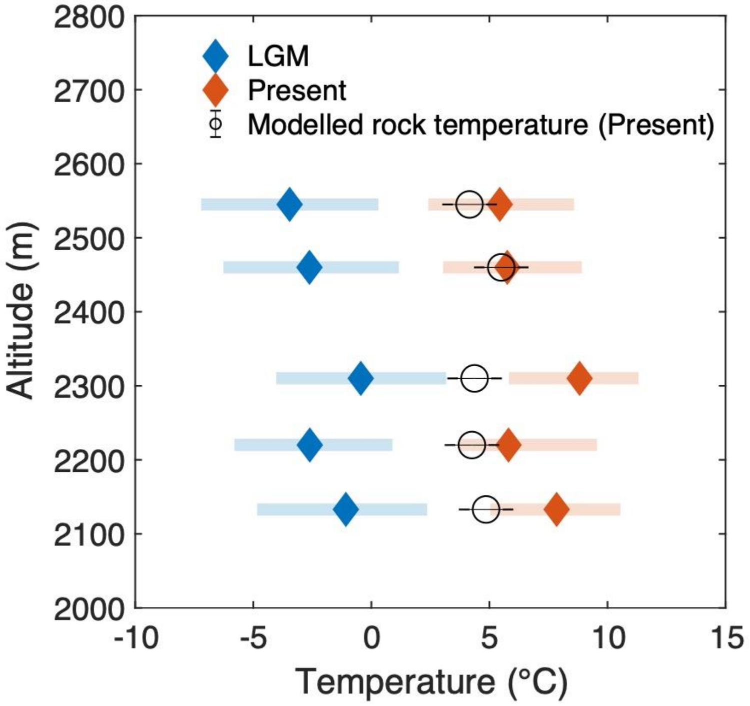

<u>Figure 2:</u> Temperature difference between LGM temperature and present-day temperature. The blue and red diamonds depict temperature at the end of the LGM and present-day respectively inferred using thermoluminescence, and the black circles depict present-day temperatures estimated from a statistical relationship between air temperature and measured rock temperature (Supplementary Materials).

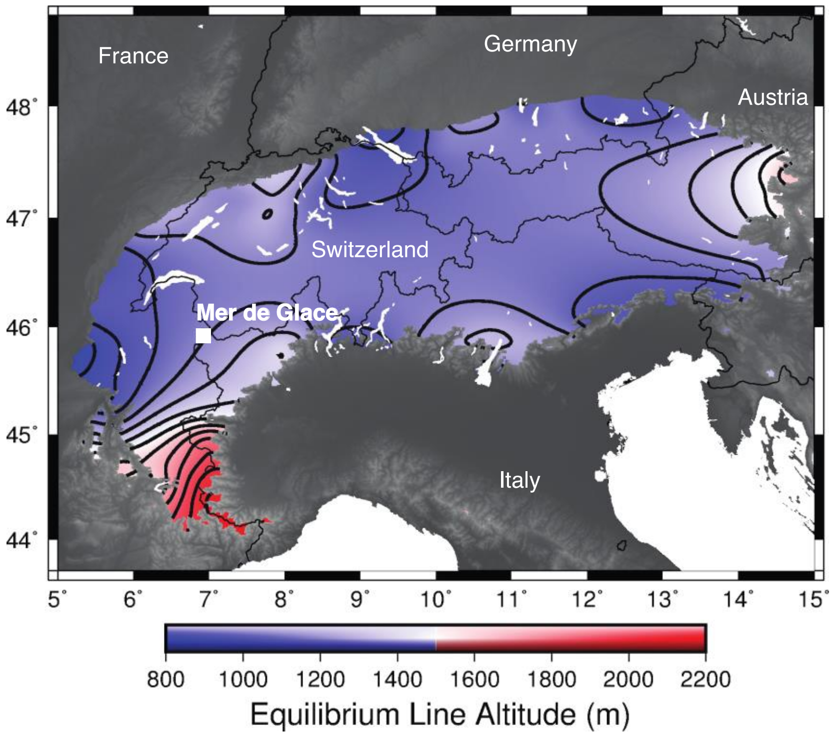

<u>Figure 3:</u> LGM Equilibrium Line Altitude (ELA) inferred from the inversion of the observed LGM ice extent (*24*). The white square shows the location of the Mer de Glace. The thin black lines depict the political borders. The thick black line are 100 m contour lines of ELA. For this inversion β is equal to 0.01 1/a and c to 0.25 m/a, which corresponds to a temperature difference between the LGM and the present at the Mer de Glace equal to 8.5 °C.

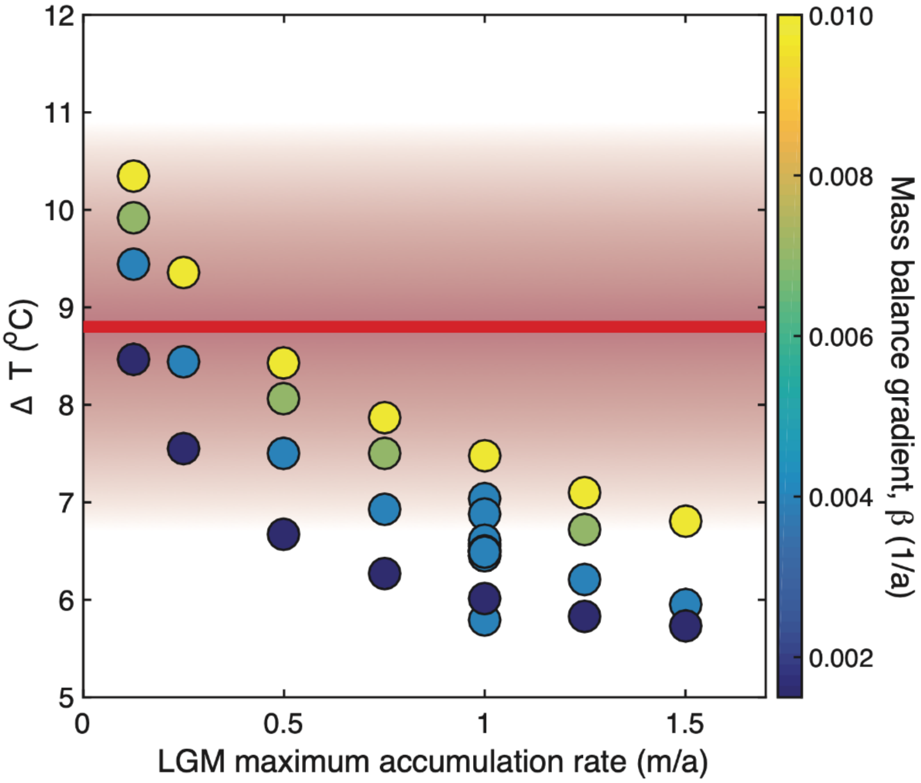

<u>Figure 4:</u> LGM accumulation rates and temperature difference at the Mer glace inferred from the inversion the LGM ice extent into ELAs. The dots depict the temperature difference between the end of the LGM and the present inferred for individual inversion of ice extent into an ELA field (Supplementary Materials). The color associated with each dot represents the mass balance gradient used for each individual inversion. The red line is the temperature difference inferred using thermoluminescence and its error.

Supplementary Materials for

Last Glacial Maximum temperature in the Alps quantified using luminescence paleothermometry

Rabiul Biswas[1], Vjeran Višnjević[1], Florence Magnin[2], Benjamin Lehmann[1], Georgina King[1], Frédéric Herman[1]

Corresponding author: frederic.herman@unil.ch

[1]: Institute of Earth Surface dynamics, University of Lausanne, Switzerland

[2]: Laboratoire EDYTEM, Université Savoie Mont-Blanc, France

This PDF file includes:

Materials and Methods
Figs. S1 to S5
Tables S1

1. Materials

Samples: Five bedrock samples were collected at the Mer de Glace glacier (Mont Blanc massif, European Alps) at altitudes from 2133 to 2545 m. The rocks are phenocrystalline granits of the Mont Blanc massif. All the rocks were collected from glacially eroded bedrock surfaces (*26*). The sample were located between the ice-surface elevations of the Little Ice Age (LIA) and the LGM (*26*). All the samples were recently dated using ^{10}Be terrestrial cosmogenic nuclide and OSL surface exposure dating simultaneously (Lehmann et al., 2020). The top four samples were exposed since the end of the LGM about 17 kyr ago (*25-26*). Only the bottom sample was exposed between the LGM and the Younger Dryas about 12 kyr ago. The location of the samples is shown in Figure 1.

2. Methods

2.1 Thermoluminescence thermometry

Thermoluminescence of feldspar: Luminescence paleothermochronometry is a recently established technique that is based on the Quaternary dating method of thermoluminescence (TL) dating (*32*). TL dating relies on the time-dependent accumulation of electrons in crystal defects that occurs when certain minerals, including feldspar, are exposed to ionizing radiation from naturally occurring radionuclides (e.g., U, Th, and K) as well as cosmic rays. The targeted trapped charge population is thermally sensitive, which can be exploited to extract thermal histories of rocks. The idea was first introduced in the sixties for terrestrial applications (*33*) and seventies for lunar samples from the Appolo 12 mission (*34-35*). It was only revived and further developed recently for terrestrial applications (*27*). Biswas et al. (*27,36*) showed that thermoluminescence signals exhibit a continuum of thermal stability. Each thermal stability range correspond to a paleothermometer. The combination of several paleothermometer enables the reconstruction of past temperature histories of rocks with great precision.

<u>Theory:</u> TL of feldspar can be described with a rate equation that encapsulates the process of populating traps with electrons in response to environmental ionizing radiation and the processes of electron escape through thermal and athermal processes. We briefly outline the kinetic model here. The reader is referred to Biswas et al. (2020) (*27*) for further information.

The rate equation for the trapped charge population of a specific trapping center, with single trap depth (E), frequency factor (s), and athermal fading parameter (ρ'; *37-38*) is as follows:

$$\frac{d}{dt}\left(\bar{n}(r',t)\right) = \frac{\dot{D}}{D_0}\left(1-\bar{n}(r',t)\right)^a - se^{-\frac{E}{kT}}\left(\bar{n}(r',t)\right)^b - \tilde{s}e^{-\rho'^{-\frac{1}{3}}r'}\bar{n}(r',t) \quad (1)$$

where $\bar{n}$ is equal to n/N (where n is the number of trapped electrons at time t and temperature T, and N is the total number of available traps), $\dot{D}$ is the dose rate due to ambient radioactivity (Gy kyr^{-1}), D_0 is the characteristic dose (Gy), a and b are the kinetic orders of trapping and thermal detrapping respectively, E is the trap depth or activation energy (eV), s and $\tilde{s}$ are the thermal and athermal frequency factor respectively (s^{-1}), $\rho'$is the dimensionless athermal fading rate and r' is a dimensionless distance that characterizes the probability of athermal escape (*38*). A key element is that a, b, $\dot{D}$, D_0 , E , s and ρ' are constrained from laboratory experiments for each sample (Biswas et al., 2018; 2020).

To account for athermal loss, i.e., anomalous fading (*39*), the total number of trapped electrons at any instant $\bar{n}(t)$ is obtained by integrating over the whole range of dimensionless distances (0< r'<2; *40*) over which electrons can athermally escape;

$$\bar{n}(t) = \int_0^\infty p(r')\bar{n}(r',t)dr' \qquad (2)$$

where $p(r')$ is the probability of nearest recombination center at a distance between r' and r'+$dr'$and expressed as $p(r')dr' = 3r'^2 e^{r'^3} dr'$ (*38*).

This model was validated using rocks from the KTB borehole and applied to samples from Namche Barwa (*36*), which gave results in agreement with other studies from the same area (*41*).

It has been established that TL of feldspar arises from a continuous distribution of trap energies (*36, 42-45*) and that the TL processes is reflected by the sum of a large number of traps (*36, 44*); all follow the process described by Equation 1. The kinetic parameters are constrained from laboratory-controlled experiments (*27,36*).

Sample preparation: The samples were prepared following the method reported in (*47*). The light exposed outer layer (>2 cm from the surface) was removed using a diamond saw under subdued red-light conditions with constant water flow to avoid frictional heating. The interior part of the sample was gently crushed with a mortar and pestle and sieved to separate the 150–250 µm grain size. The samples were sequentially treated with 10% HCl and 30% H_2O_2 to remove carbonate and organic matter respectively. Once dried, the magnetic fractions were separated and removed using a hand magnet. The K-feldspar fraction was removed by density separation (<2.58 gm/cm^3) using sodium polytungstate. The grains were mounted on stainless steel discs using Silko-spay. Small aliquots of 2 mm diameter (containing ~100 grains) were prepared because the analyzed feldspars were very bright.

Luminescence measurements: The TL measurements were made using a Risø TL/OSL reader (*48*) equipped with a ^{90}Sr/^{90}Y irradiation source (~ 0.24 Gy/s) at the University of Lausanne. A heating rate of 1 °C/s was used, under constant flow of N_2 gas. The TL emission was restricted to violet-blue (395±30 nm) using a filter combination of BG3 and BG39. A sensitivity correction was applied to the measurements following Biswas et al. (2020). The natural TL or present-day trapped charge population was measured and a sensitivity correction was applied to the measurements following (*27*).

<u>Inversion of TL data into thermal histories:</u> We use a Bayesian approach to invert TL data ($\bar{n}_o$) into thermal histories. The approach consists of generating a large number of random thermal histories (300,000) and predict $\bar{n}_p$ for each thermal history using Equation 1. We then compare the predicted value to the observed one, $\bar{n}_o$, and select the thermal histories that provide the best fit to the data. From the selected path, we can then build a probably density function and estimate temperatures at the LGM and the present (*27*).

We assume that the shape of the temperature histories follows the ice core δ^{18}O Greenland record (*48*). All the existing records from the Alps follow the Greenland oxygen isotope record (*30*). However, the records are not continuous during the last 20 kyr, and how temperature varied is unknown and. Here we scale the continuous δ^{18}O record from Greenland by varying the minimum temperature (i.e., temperature at ~17 kyr ago) between -20 and 20 °C and the maximum amplitude of the temperature change between between 0 and 30 °C (i.e., the difference between minimum the temperature and the maximum temperature).

For each thermal history, we assess the quality of fit to the data using the following misfit function (*49*)

$$\chi = \frac{1}{l}\sum_{i=1}^{l}\left[\frac{1}{2}\times\frac{\bar{n}_o}{\sigma_{\bar{n}_o}}\times\log\frac{\bar{n}_p}{\bar{n}_o}\right]^2 \qquad (3)$$

from which we estimate a likelihood, $\mathcal{L}$,

$$\mathcal{L} = \exp(-\chi) \qquad (4)$$

where *l* is the number of TL signals (or thermometers) selected in TL temperature range (*27*), (here *l*=4), $\sigma_{\bar{n}_o}$ is the measured error on $\bar{n}_o$. To account for the measurement uncertainties in the kinetic parameters, we randomly pick the kinetic parameters within its error range for each thermal history. We run the model for large number of thermal histories (300,000 iterations) to ensure that we explore a wide range of possible solutions.

Finally, the thermal histories that best fit the data are selected using a rejection algorithm that satisfies the criterion $\mathcal{L} > R$, where R is a random number between 0 and 1. A probability density distribution is then constructed by counting the number of accepted thermal histories passing through grid cells, which are generated by dividing the time-temperature space (0-100 kyr ago and -50 to 50 °C) into 100×100 cells. This approach is commonly used in different thermochronometric studies (*36,41,46, 51-52*). The inversion results for all the samples are shown in Figure S1.

We constrain the temperature at present and at the end of LGM, 17 kyr ago. As mentioned above, the timing of end of LGM or complete removal of icecap is partly uncertain. The top four samples were most like exposed since 17 kyr ago (Lehmann et al., 2020). The bottom sample was exposed sometime between 17 to 12 kyr ago (Lehmann et al., 2020). To assess the influence it may have on our interpretation, we calculated the temperature at different times (20, 17, 15 and 12 kyr ago), which is shown in Figure S2(A-B). It is important to note that temperature is nearly the same for the deglaciation period of 20-15 kyr ago, which is expected as we use the Greenland δ^{18}O record. As result, the estimated temperature at the end of the LGM remain relatively insensitive to the timing of deglaciations. However, the temperature offset is significantly lower if the deglaciation occurred only at 12 kyr ago, which would only apply to the lowest sample.

<u>Mean temperature difference:</u> To estimate the mean temperature difference between the LGM and the present in the Mer de Glace area, we calculate the weighted mean and standard deviation using the results from the inversion for the five analyzed samples and assuming that all the errors are independent. The results are shown in Figure S2(E-H).

2.2 Temperature model

A linear regression model (*29*) that calculates the difference, i.e., surface offset, between the rock surface and the air temperature for a given potential incoming solar radiation (PSIR) was fitted with surface temperature measurements collected at the Aiguille du Midi (3842 m, Mont Blanc massif) between 2008 and 2018.

The surface temperature was measured at a hourly time step at a depth of 10 cm and then aggregated into mean annual values. Three measurement points were taken in the south-exposed face of the Aiguille du Midi, two on the east face, two on the north face and two on the west face in sub-vertical rock walls. In addition, temperature measured at 30 cm in three 10-m-deep boreholes were also used (one on the north-west exposed rock face, one on the north-east and one on the south-east) in slopes angles ranging from 55 to 80°. The last three sensors and one of the three sensors installed on the south face are usually covered by snow during winter due to local topographical setting while all other sensors remain in snow free conditions. Snow cover influences the registered surface temperature due to both its thermal insulation effect and its high albedo. Thereby, the surface temperature sample is representative of most alpine bedrock settings. The measurements installations and settings as well as the rock surface temperature characteristics are reported in (*29*). For this study, a total of 78 mean annual rock surface temperature points were available to calibrate the regression model.

The air temperature has been measured continuously on top of the Aiguille du Midi by Météo France since 2007. Daily air temperature values were also aggregated in annual mean temperature. Finally, the PISR was calculated for a 1-m-resolution DEM of the Aiguille du Midi, which was built up from a terrestrial laser-scanning point cloud (acquired by L. Ravanel and processed by E. Ployon and F. Magnin) using the Spatial Analyst toolbox from ArcGIS® (ESRI). As a potential value, the solar radiation was calculated at a hourly time step over one full year assuming no atmosphere (transmittance value of 1) and then converted into a mean annual value. PISR values were then extracted at location of surface temperature from the 1 m resolution PISR map. The following model was then calibrated: SO = 0.0023×PISR + 0.75. The results are shown in Figure S3.

The model was used to calculate possible surface offset at bedrock sample locations by mapping the PISR over a 2 m DEM generated from a point cloud acquired and provided by the IGE (University Grenoble-Alpes, CNRS, IRD) within the GlacioClim observation service (Fig. S4). Similarly to model calibration, the PISR was extracted at bedrock sample location to calculate the offset with the linear regression.

Finally, we estimated the present temperature at each sample location by adding the temperature offset to the estimated air temperature. The air temperature at each sample location was estimated using the mean annual air temperature in Chamonix and scaling it with altitude assuming a temperature lapse rate equal to 0.55 °C per 100 meter.

2.3 Inversion of paleo ice-extents into ELA fields

We use a formal inversion approach (*22*) to invert the observed ice extent into spatially variable Equilibrium Line Altitudes (ELAs). This approach consists of imposing a mass balance rate to an ice flow model and find the range of ELA fields that can reproduce the observed LGM ice-extent.

To simulate the ice flow, we solve the shallow ice approximation (*51*) and account for the effect of flexural isostasy to adjust the elevation due to the flexure of the lithosphere under the weight of the modelled ice-cap. The ensemble of equations being solved are presented in (*22,52*). For the mass balance rate, M, we assume a standard linear function (*54-57*):

$$M = \min\big(\beta\big(S(x,y) - ELA(x,y)\big), c\big) \qquad (5)$$

where S is the ice surface elevation, ELA is the elevation of the equilibrium line altitude, β is the mass balance gradient and c is the maximum accumulation rate. To keep the number of unconstrained parameters low, we assume that β is identical for the ablation and accumulation areas, even though the mass balance gradient is often different in the accumulation and ablation zones.

The inversion then consists of running the ice flow model iteratively until a spatially varying ELA field that enables to fit the observed ice extent is found. To be able to run a large number of models, the code is accelerated using Graphic Processing Units (*52*). The model is run until steady state and we assume that the maximum ice extent was synchronous for all the observed moraines, which is reasonable given the dating errors of about 2 to 4 ka (*25*). We regularize the problem by assuming a smooth solution using a Tikhonov regularization (*58-59*). Each inversion includes about 1000 forward ice flow models.

Višnjević et al. (2020) (*22*) repeated the inversion 27 times for a set of possible β and c. They also varied the varied the sliding parameter, the elastic thickness and the inversion parameters. We complemented these results with 12 additional inversions to fully explore the range of possible solutions and in particular quantify the tradeoff that exists between precipitation and temperature. All the inversion results reported here were made assuming that the mass balance gradient, β, is lower or equal to the one observed at present, i.e., 0.01 1/a (*60*). c was varied between 0.25 and 2 m/a. The maximum winter accumulation rate observed at present is equal to 1.71 m/a (Huss et al., 2008).

We use an existing LGM ice extents for the Alps (*24*) and the SRTM data for topography. The ensemble of model parameters is reported in (*22*).

Finally, we convert the inferred the ELA field into temperatures and precipitation rates at the Mer de Glace (Fig. 4). The difference of altitude between the LGM and present ELA is converted into a temperature difference using the observed altitudinal temperature lapse rate (0.55°C per 100 m) for each set of β and c. The difference of precipitation is simply taken as the difference between c and the currently observed winter accumulation rate. Although we do not account for local effects such as surrounding topography, we find a general agreement in temperature changes throughout the Alps.

2.4 Ice extents for different tempetures

To illustrate the effect of temperature change on the ice extent we ran three forward simulations assuming that the temperature was 8.5, 5 and 3.5 °C colder than present, β is equal to 0.01 1/a and c is equal to 0.25 m/a, so 85% drier than at present. The results show that the ice was not that different between 3.5 and 5 °C and considerably larger for 8.5 °C (Fig. S5).

Supplementary Materials References

32. Aitken, M.J. *Thermoluminescence dating* (1985).
33. Ronca, L.B. & Zeller, E.J.. Thermoluminescence as a function of climate and temperature. *American Journal of Science*, *263*(5), 416-428 (1965).
34. Durrani, S.A., Prachyabrued, W., Christo-Doulides, C., Fremlin, J.H., Edgington, J.A., Chen, R. & Blair, I.M. Thermoluminescence of Apollo 12 samples: implications for lunar temperature and radiation histories. In *Lunar and Planetary Science Conference Proceedings*, **3**, 2955-2969 (1972).
35. Durrani, S.A., Khazal, K.A.R. & Ali, A.. Temperature and duration of the shadow of a recently-arrived lunar boulder. *Nature*, **_266_(5601)**, 411-415 (1977).
36. Biswas, R.H., Herman, F., King, G.E. & Braun, J. Thermoluminescence of feldspar as a multi-thermochronometer to constrain the temporal variation of rock exhumation in the recent past. *Earth and Planetary Science Letters*, ***495***, 56-68 (2018).
37. Tachiya, M. & Mozumder, A. Decay of trapped electrons by tunnelling to scavenger molecules in low-temperature glasses. *Chemical Physics Letters*, **_28_(1)**, 87-89 (1974).
38. Huntley, D.J.. An explanation of the power-law decay of luminescence. *Journal of Physics: Condensed Matter*, **_18_(4)**, 1359-1365 (2006).
39. Wintle, A.G. Anomalous fading of thermo-luminescence in mineral samples. *Nature*, **_245_(5421)**, 143-144 (1973).
40. Kars, R.H., Wallinga, J. & Cohen, K.M. A new approach towards anomalous fading correction for feldspar IRSL dating—tests on samples in field saturation. *Radiation Measurements*, **_43_(2-6)**, 786-790 (2008).
41. King, G.E., Herman, F. & Guralnik, B. Northward migration of the eastern Himalayan syntaxis revealed by OSL thermochronometry. *Science*, **_353_(6301)**, 800-804 (2016a).
42. Duller, G.A.T. Behavioural studies of stimulated luminescence from feldspars. *Radiation Measurements*, **_27_(5-6)**, 663-694 (1997).
43. Grün, R. & Packman, S.C. Observations on the kinetics involved in the TL glow curves in quartz, K-feldspar and Na-feldspar mineral separates of sediments and their significance for dating studies. *Radiation measurements*, **_23_(2-3)**, 317-322 (1994).

44. Pagonis, V., Morthekai, P. & Kitis, G. Kinetic analysis of thermoluminescence glow curves in feldspar: evidence for a continuous distribution of energies. *Geochronometria*, ***41*(2)**, 168-177 (2014).
45. Strickertsson, K.. The thermoluminescence of potassium feldspars—glow curve characteristics and initial rise measurements. *Nuclear Tracks and Radiation Measurements*, ***10*(4-6)**, 613-617 (1985).
46. King, G.E., Herman, F., Lambert, R., Valla, P.G. & Guralnik, B. Multi-OSL-thermochronometry of feldspar. *Quaternary Geochronology*, ***33***, 76-87 (2016b).
47. Bøtter-Jensen, L., Thomsen, K.J. & Jain, M. Review of optically stimulated luminescence (OSL) instrumental developments for retrospective dosimetry. *Radiation Measurements*, ***45*(3-6)**, 253-257 (2010).
48. Svensson, A., Andersen, K.K., Bigler, M., Clausen, H.B., Dahl-Jensen, D., Davies, S.M., Johnsen, S.J., Muscheler, R., Parrenin, F., Rasmussen, S.O. & Roethlisberger, R. A 60 000 year Greenland stratigraphic ice core chronology. *Climate of the Past*, **4**, 44-57 (2008)
49. Wheelock, B., Constable, S. & Key, K.. The advantages of logarithmically scaled data for electromagnetic inversion. *Geophysical Journal International*, ***201*(3)**, 1765-1780 (2015).
50. Herman, F., Rhodes, E.J., Braun, J. & Heiniger, L. Uniform erosion rates and relief amplitude during glacial cycles in the Southern Alps of New Zealand, as revealed from OSL-thermochronology. *Earth and Planetary Science Letters*, ***297*(1-2)**, 183-189 (2010).
51. Gallagher, K.. Transdimensional inverse thermal history modeling for quantitative thermochronology. *Journal of Geophysical Research: Solid Earth*, ***117*(B2)** (2012).
52. Višnjević, V., Herman, F. & Podladchikov, Y. Reconstructing spatially variable mass balances from past ice extents by inverse modeling. *Journal of Glaciology*, ***64*(248)**, 957-968 (2018).
53. Hutter, K. *Theoretical glaciology: material science of ice and the mechanics of glaciers and ice sheets.* Springer (1983).
54. Meier, M.F. Proposed definitions for glacier mass budget terms. *Journal of Glaciology*, ***4*(33)**, 252-263 (1962).
55. Mayo, L.R. Glacier mass balance and runoff research in the USA. *Geografiska Annaler: Series A, Physical Geography*, ***66*(3)**, 215-227 (1984).
56. Oerlemans, J., & N. C. Hoogendoorn. Mass-balance gradients and climatic change. *Journal of Glaciology,* **35(121)**, 399-405 (1989).
57. Giesen, R.H. & Oerlemans, J. Calibration of a surface mass balance model for global-scale applications. *The Cryosphere*, ***6*(6)**, 1463-1481 (2012).
58. Tikhonov, A.N. On the solution of ill-posed problems and the method of regularization. In *Doklady Akademii Nauk*, Russian Academy of Sciences, **151(3)**, 501-504. (1963).
59. Aster, R.C., Borchers, B. & Thurber, C.H.. *Parameter estimation and inverse problems*. Elsevier (2018)
60. Rabatel, A., Dedieu, J.P. & Vincent, C. Using remote-sensing data to determine equilibrium-line altitude and mass-balance time series: validation on three French glaciers, 1994–2002. *Journal of Glaciology*, ***51*(175)**, 539-546 (2005).
61. Huss, M., Bauder, A., Funk, M. and Hock, R. Determination of the seasonal mass balance of four Alpine glaciers since 1865. *Journal of Geophysical Research: Earth Surface*, ***113*(F1)** (2008).

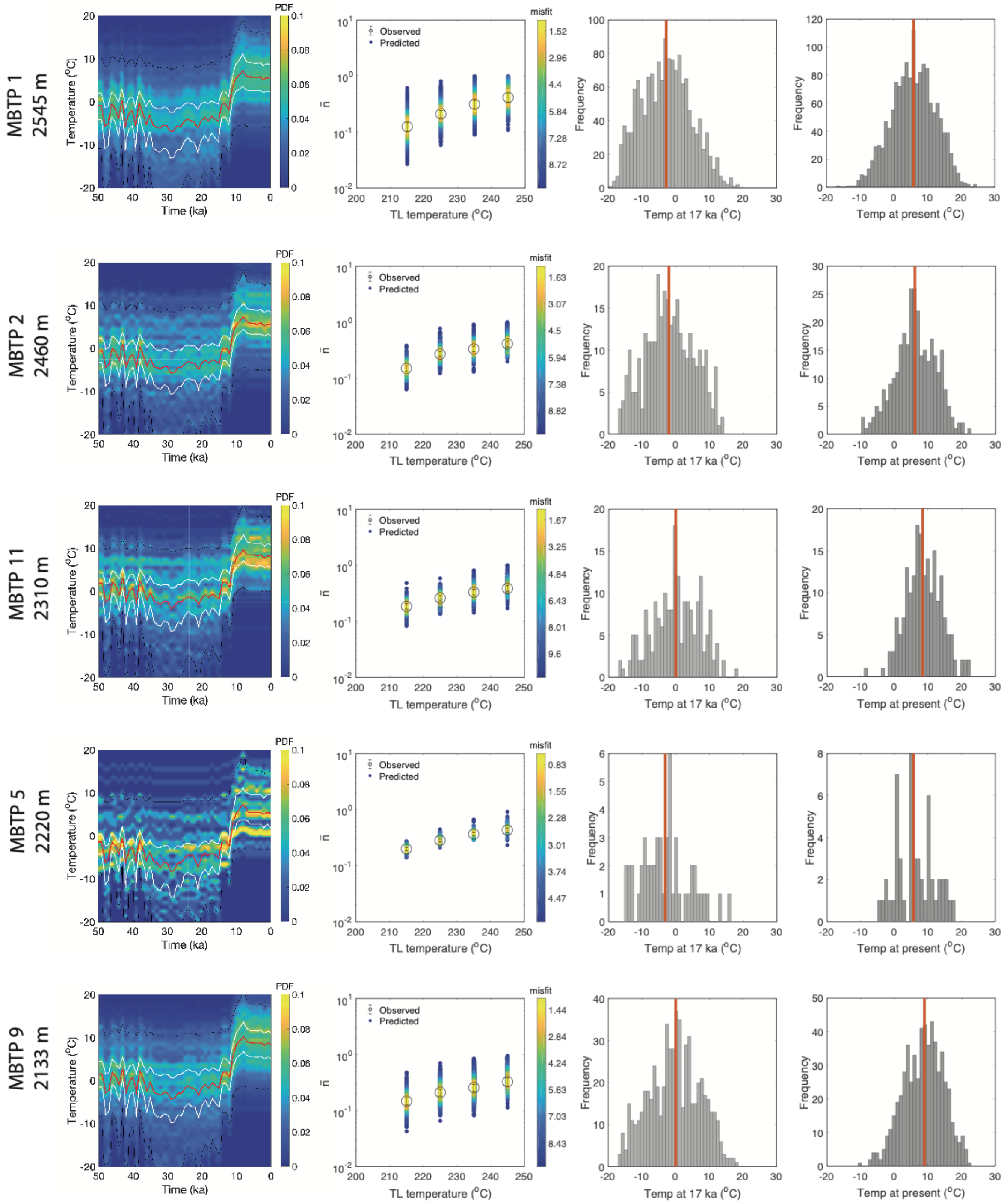

<u>Figure S1:</u> Inversion of thermoluminescence data. The first column corresponds to inferred probability density functions of the temperature histories. The second column shows the fit to the observed data, $\bar{n}_o$. The third and fourth columns depict the 1-d marginals of probability density functions of temperature at the end of the LGM and the present, respectively.

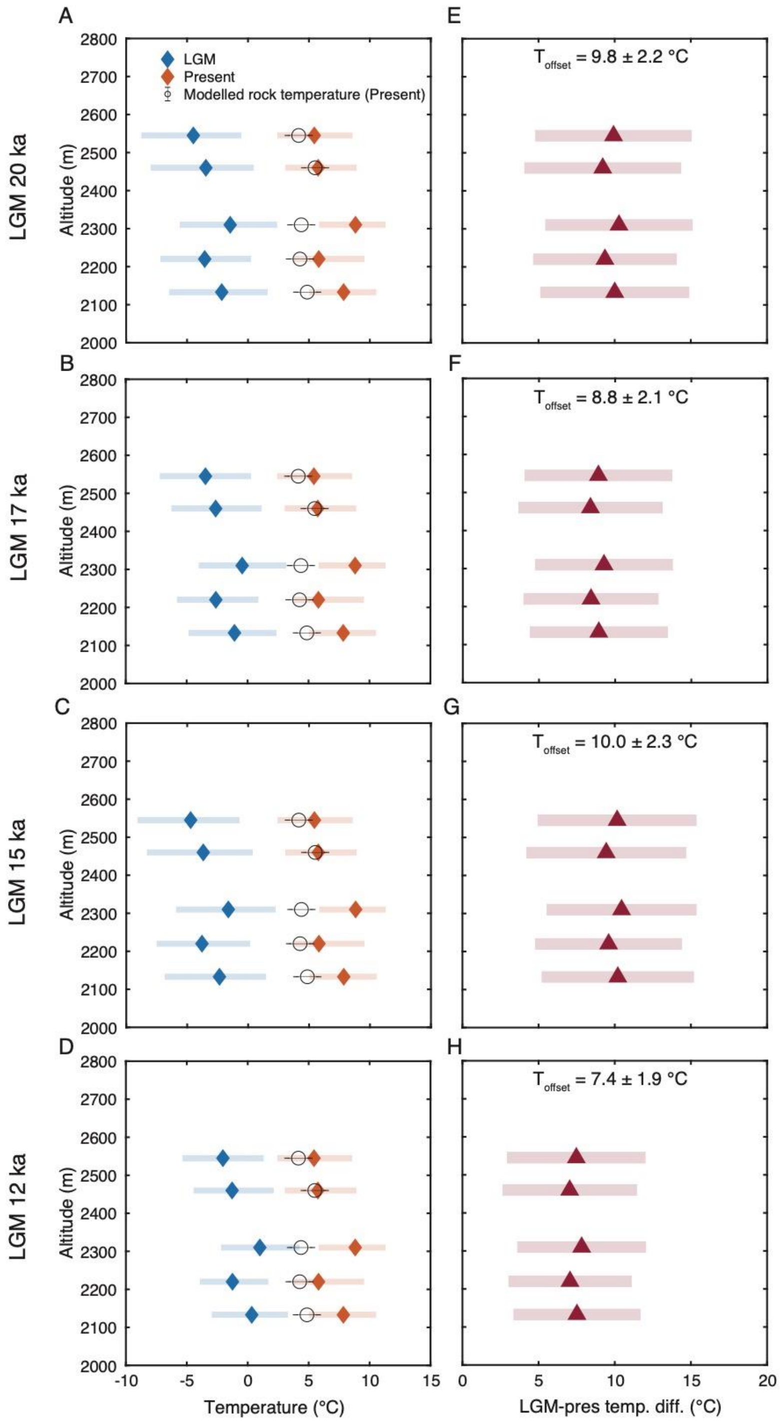

<u>Figure S2:</u> Estimated temperature differences at different times (20, 17, 15 and 12 kyr ago). (A) to (D) are the estimated temperatures. (E) to (H) are the estimated temperature differences between the LGM and the present. The results show that the temperature differences between the LGM and today was similar at 20, 17 and 12 kyr ago.

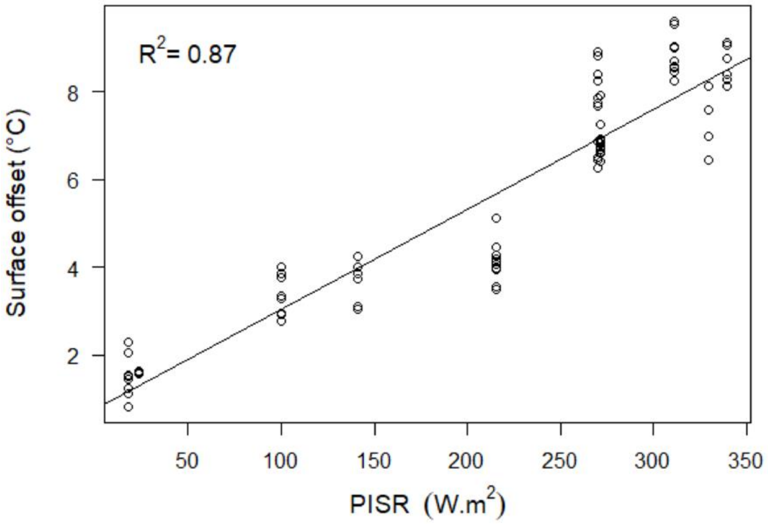

Figure S3: **Estimated temperature offset between air and rock temperature.** The Linear regression model explaining the Surface Offset with the potential incoming solar radiation (PISR) where the samples were collected (Fig. 1).

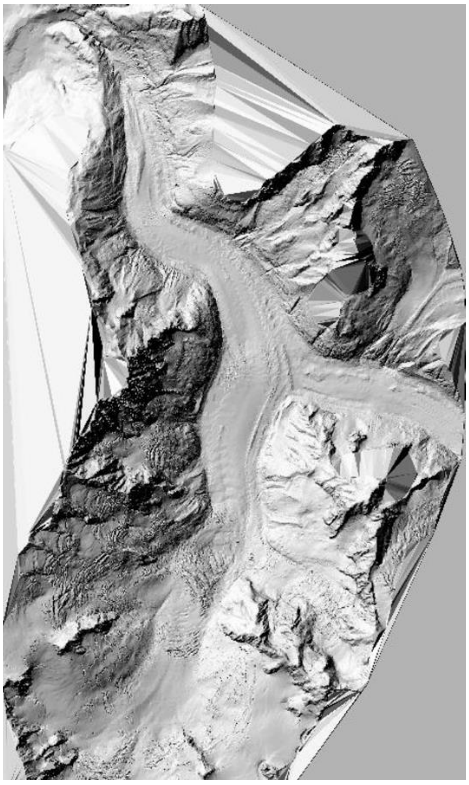

Figure S4: Hillshade of the 2-m resolution DEM generated for the Mer de Glace and used to estimate the offset temperature (Fig. S3).

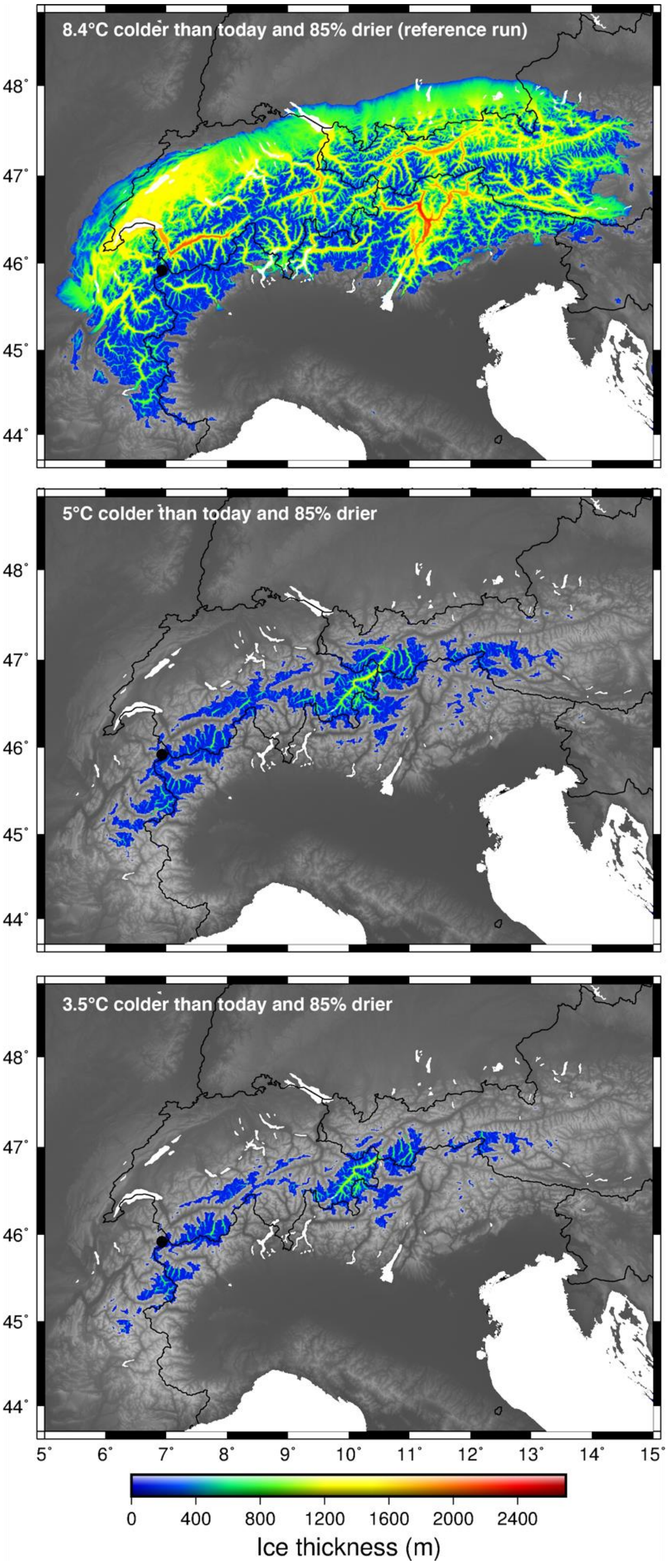

<u>Figure S5:</u> Ice thickness for 3 forward runs assuming that β is equal to 0.01 1/a and c is equal to 0.25 m/a.

<u>Table S1.</u> Thermoluminescence results and parameters. The $\dot{D}$ values are from Lehmann et al. (2020). We do not report the errors for the thermal decay parameters (E, s and b). The estimated assuming an arbitrary error of 5%.

		Growth			Thermal decay			Athermal decay	Natural TL ($\overline{n}_{obs}$)		
	TL (°C)	$\dot{D}$ (Gy/ ka) *	D_0 (Gy)	a	E (eV)	$\log_{10}(s)$	b	$\log_{10}(\rho')$	Uncorrected	NCF	Corrected
MBTP 1	210-220	7.39 ± 0.16	766 ± 51	1.00 ± 0.09	1.24	11.62	1.46	-6.02 ± 0.08	0.17 ± 0.03	1.36 ± 0.04	0.13 ± 0.02
	220-230		690 ± 46	1.00 ± 0.11	1.28	11.69	1.45	-6.29 ± 0.14	0.28 ± 0.04	1.34 ± 0.03	0.21 ± 0.03
	230-240		638 ± 43	1.00 ± 0.13	1.31	11.75	1.45	-7.10 ± 0.94	0.41 ± 0.07	1.31 ± 0.03	0.31 ± 0.05
	240-250		559 ± 40	1.00 ± 0.26	1.35	11.79	1.45	<-20 ± 0.00	0.53 ± 0.09	1.29 ± 0.03	0.41 ± 0.07
MBTP 2	210-220	7.35 ± 0.15	796 ± 32	1.00 ± 0.03	1.25	11.73	1.47	-6.36 ± 0.20	0.23 ± 0.03	1.51 ± 0.02	0.15 ± 0.02
	220-230		500 ± -	1.00 ± 0.00	1.29	11.82	1.46	-6.64 ± 0.39	0.40 ± 0.04	1.48 ± 0.02	0.27 ± 0.03
	230-240		644 ± 27	1.05 ± 0.19	1.32	11.89	1.46	-7.62 ± 3.74	0.48 ± 0.06	1.46 ± 0.03	0.33 ± 0.04
	240-250		559 ± 29	1.18 ± 0.24	1.36	11.96	1.46	<-20 ± 0.00	0.59 ± 0.07	1.43 ± 0.03	0.41 ± 0.05
MBTP 5	210-220	7.73 ± 0.16	770 ± 30	1.00 ± 0.04	1.23	11.47	1.51	<-20 ± 0.00	0.36 ± 0.02	1.82 ± 0.03	0.20 ± 0.01
	220-230		710 ± 24	1.00 ± 0.00	1.27	11.54	1.51	<-20 ± 0.00	0.51 ± 0.03	1.80 ± 0.03	0.28 ± 0.02
	230-240		631 ± 20	1.02 ± 0.13	1.30	11.59	1.51	<-20 ± 0.00	0.65 ± 0.05	1.78 ± 0.03	0.37 ± 0.03
	240-250		559 ± 18	1.07 ± 0.13	1.34	11.63	1.51	<-20 ± 0.00	0.76 ± 0.07	1.76 ± 0.03	0.43 ± 0.04
MBTP 9	210-220	7.07 ± 0.15	773 ± 41	1.00 ± 0.03	1.25	11.63	1.49	-6.13 ± 0.09	0.26 ± 0.03	1.73 ± 0.08	0.15 ± 0.02
	220-230		680 ± 37	1.00 ± 0.01	1.29	11.72	1.49	-6.18 ± 0.10	0.36 ± 0.05	1.72 ± 0.08	0.21 ± 0.03
	230-240		625 ± 40	1.18 ± 0.33	1.32	11.79	1.49	-6.33 ± 0.17	0.44 ± 0.06	1.71 ± 0.09	0.26 ± 0.04
	240-250		502 ± 36	1.10 ± 0.27	1.36	11.85	1.49	-6.51 ± 0.24	0.56 ± 0.08	1.70 ± 0.09	0.33 ± 0.05
MBTP11	210-220	8.14 ± 0.17	707 ± 20	1.00 ± 0.01	1.24	11.52	1.49	<-20 ± 0.00	0.33 ± 0.03	1.81 ± 0.14	0.18 ± 0.02
	220-230		660 ± 18	1.00 ± 0.11	1.28	11.59	1.49	<-20 ± 0.00	0.46 ± 0.03	1.79 ± 0.14	0.26 ± 0.03
	230-240		593 ± 19	1.00 ± 0.13	1.32	11.65	1.49	<-20 ± 0.00	0.59 ± 0.04	1.77 ± 0.15	0.33 ± 0.04
	240-250		527 ± 18	1.00 ± 0.07	1.35	11.69	1.49	<-20 ± 0.00	0.67 ± 0.06	1.75 ± 0.15	0.38 ± 0.05